



Charge radii of Ca isotopes and correlations

G. Co' ^{1,2}, M. Anguiano,³ and A. M. Lallena ³

¹*Dipartimento di Matematica e Fisica "E. De Giorgi", Università del Salento, I-73100 Lecce, Italy*

²*INFN Sezione di Lecce, Via Arnesano, I-73100 Lecce, Italy*

³*Departamento de Física Atómica, Molecular y Nuclear, Universidad de Granada, E-18071 Granada, Spain*



(Received 27 January 2022; accepted 4 March 2022; published 17 March 2022)

We study the effects of short- and long-range correlations on the charge radii of Ca isotopes. We start our investigation with an independent particle model consisting of Hartree-Fock plus Bardeen-Cooper-Schrieffer calculations with finite-range effective nucleon-nucleon interactions of Gogny type. The short-range correlation effects are evaluated by considering all the terms of a cluster expansion containing a single correlation line. The long-range correlations are taken into account by including the coupling with the quasiparticle random phase approximation phonons. While the effects of the short-range correlations are negligible, those of the long-range correlations largely modify the independent particle model results and improve the agreement with the experimental data.

DOI: [10.1103/PhysRevC.105.034320](https://doi.org/10.1103/PhysRevC.105.034320)

I. INTRODUCTION

In these last few years, the measurement of several isotope shifts completed the information about the charge radii of Ca nuclei. Garcia Ruiz *et al.* [1] measured the isotope shifts of the neutron rich ^{49,51,52}Ca nuclei using laser spectroscopy and Miller *et al.* [2] investigated the proton rich ^{36,37,38}Ca isotopes with similar experimental techniques. These new data have been used to derive the values of the charge radii of these nuclei.

The behavior of the experimental values of the charge radii shows a steep enhancement for nuclei with $A > 48$. This behavior is not described by several independent particle models [1–3]). It has been shown [2] that by using elaborate energy functionals, containing a large number of free parameters [4–6], it is possible to reproduce the full set of experimental data. However, the physics simulated by these new functionals is difficult to disentangle.

In this work we attack the problem by using a more traditional independent particle model, which in our case consists in Hartree-Fock (HF) plus Bardeen-Cooper-Schrieffer (BCS) calculations, and we study the effects of the correlations. We consider short-range correlations related to the strongly repulsive core of the nucleon-nucleon interaction and long-range correlations generated by the coupling of collective nuclear excitations to the single-particle degrees of freedom.

This work is organized as follows. Section II is devoted to present some details of the various theoretical approaches used in our calculations. In Sec. III we show our results, which are discussed in Sec. IV where we also present our conclusions.

II. THEORETICAL APPROACHES

The goal of our study is the evaluation of the root mean square (r.m.s.) radii of nuclear density distributions

$\rho_\alpha(r)$:

$$R_\alpha = \left[\frac{\int_0^\infty dr r^4 \rho_\alpha(r)}{\int_0^\infty dr r^2 \rho_\alpha(r)} \right]^{\frac{1}{2}}. \quad (1)$$

Proton and neutron r.m.s. radii are obtained by considering the (pointlike) proton, ρ_p , and neutron, ρ_n , density distributions, which are defined as

$$\rho_\alpha(\mathbf{r}) = \frac{A}{\langle \Psi | \Psi \rangle} \langle \Psi | \sum_j' \delta(\mathbf{r} - \mathbf{r}_j) | \Psi \rangle, \quad \alpha \equiv p, n, \quad (2)$$

where $|\Psi\rangle$ is the state describing the full nucleus, which has A nucleons (Z protons and N neutrons). In the above equation, and in all the following ones, \sum_j' indicates that the sum is limited either to the protons or to the neutrons as indicated by the subindex α . Mass r.m.s. radii are obtained by using the mass density distributions, $\rho_m = \rho_p + \rho_n$. We calculate the charge r.m.s. radii by inserting in Eq. (1) the charge distributions, ρ_c obtained by folding the (pointlike) proton densities, ρ_p , with the charge proton form factor. We used a dipole parametrization of this form factor [7], having verified that other, more complex expressions produce differences smaller than the numerical accuracy of our calculations.

The aim of the various nuclear models we adopted in our study is the evaluation of the density distributions required to calculate the r.m.s. radii.

A. Independent particle model

The starting point of our approach is the independent particle model (IPM) in which the nuclear state $|\Psi\rangle$ is described as a Slater determinant, $\Phi(1, 2, \dots, A)$, of single-particle (s.p.) wave functions. We exploit the spherical symmetry of the problem, and for the s.p. wave functions we have used the

expression [8,9]

$$\phi_\mu(\mathbf{r}) \equiv \phi_{nljm}^{m_t}(\mathbf{r}) = \mathcal{R}_{nljm}(r) \mathcal{Y}_{ljm}(\Omega) \chi_{\frac{1}{2}m_t}, \quad (3)$$

where we have indicated with n the principal quantum number, and with l , j , and m the quantum numbers identifying the orbital, the total angular momentum, and its projection on the z axis, respectively. The symbol \mathcal{Y} indicates the spin-spherical harmonics [10] and m_t the third component of the isospin.

Since we have considered nuclei without deformation, we have assumed a unique radial wave function for the same n, l, j quantum numbers, i.e., $\mathcal{R}_{nljm} \equiv \mathcal{R}_{nlj}$. In open shell nuclei the degenerate, not fully occupied, s.p. neutron state near the Fermi level is equally occupied with respect to the projection quantum number m .

The first step of our IPM calculation consisted of obtaining the s.p. radial wave functions \mathcal{R}_{nlj} by solving a set of HF equations. In a second step, we considered the pairing effects by using these HF s.p. wave functions in a BCS calculation which modifies the occupation probability, v_μ^2 , of each s.p. state. We named this IPM type of calculation HF+BCS [8,9], and, in this model, the density distributions are given by

$$\rho_\alpha^{\text{IPM}}(r) = \frac{1}{4\pi} \sum'_\mu (2j+1) v_\mu^2 [\mathcal{R}_\mu(r)]^2, \quad \alpha \equiv p, n. \quad (4)$$

The only physical input of this calculation is the effective nucleon-nucleon interaction. We consistently used the same finite-range effective nucleon-nucleon interactions of Gogny type [11] in both the HF and the BCS steps. In order to test the sensitivity of our results to the effective nucleon-nucleon interaction we carried out calculations with three different parametrizations. Two of them are the well known D1S [12] and D1M [13] interactions, and the third one is the D1ST2a, a force built by adding tensor terms to D1S [14].

B. Short-range correlations

In the IPM each nucleon is free to move independently of the presence of the other ones. On the other hand, the nucleon-nucleon interaction has a strongly repulsive core which prevents two nucleons from approaching each other at distances smaller than about 0.5 fm. This is the source of the short-range correlations (SRC).

We have evaluated the effects of the SRC by following the approach of Ref. [15], where the nuclear state is described as

$$|\Psi\rangle \equiv \Psi^{\text{SRC}}(1, 2, \dots, A) = F(1, 2, \dots, A) \Phi(1, 2, \dots, A), \quad (5)$$

with Φ indicating the IPM Slater determinant, and F a many-body correlation function which we have assumed to be of the form

$$F(1, 2, \dots, A) = \mathcal{S} \prod_{i < j} \sum_{p=1}^6 f^{(p)}(r_{ij}) O_{i,j}^{(p)}, \quad (6)$$

We indicate with \mathcal{S} a symmetrization operator, with $f^{(p)}(r_{ij})$ a two-body correlation scalar function acting on the (i, j) nucleon pair, and with $\{O^{(p)}, p = 1, \dots, 6\}$ a set of operators depending on spin, isospin, and tensor terms, classified as in the usual Urbana-Argonne sequence [16]. Specifically, we

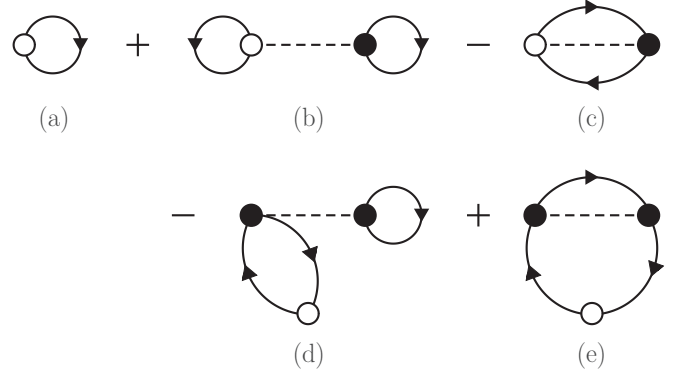


FIG. 1. The set of SRC diagrams considered in our calculations. The dashed lines indicate the correlation function h , Eq. (10), while the oriented lines represent the IPM one-body density matrices $\rho_\alpha^{\text{IPM}}(\mathbf{r}_1, \mathbf{r}_2)$, Eq. (11). The solid dots indicate a coordinate where an integration is carried out and the open ones those where the density is evaluated.

have considered operators of central type,

$$\begin{aligned} O_{ij}^{(1)} &= 1, & O_{ij}^{(2)} &= \boldsymbol{\tau}(i) \cdot \boldsymbol{\tau}(j), & O_{ij}^{(3)} &= \boldsymbol{\sigma}(i) \cdot \boldsymbol{\sigma}(j), \\ O_{ij}^{(4)} &= \boldsymbol{\sigma}(i) \cdot \boldsymbol{\sigma}(j) \boldsymbol{\tau}(i) \cdot \boldsymbol{\tau}(j), \end{aligned} \quad (7)$$

and of tensor type,

$$O_{ij}^{(5)} = S(i, j), \quad O_{ij}^{(6)} = S(i, j) \boldsymbol{\tau}(i) \cdot \boldsymbol{\tau}(j), \quad (8)$$

where $\boldsymbol{\sigma}$ indicates the spin operator, $\boldsymbol{\tau}$ the isospin operator, and $S(i, j)$ the tensor operator defined as

$$S(i, j) = 3 \frac{[\boldsymbol{\sigma}(i) \cdot \mathbf{r}_{ij}][\boldsymbol{\sigma}(j) \cdot \mathbf{r}_{ij}]}{r_{ij}^2} - \boldsymbol{\sigma}(i) \cdot \boldsymbol{\sigma}(j). \quad (9)$$

The key point of the model of Ref. [15] is the truncation of the cluster expansion of the density distribution in order to consider only those terms with a single correlation function:

$$h^{(p)}(r_{ij}) = f^{(p)}(r_{ij}) - \delta_{p,1}, \quad (10)$$

where δ is the Kronecker symbol. We show in Fig. 1 the diagrams included in the calculations. The dashed lines represent the h correlation function and the oriented lines the IPM one-body density matrix,

$$\rho_\alpha^{\text{IPM}}(\mathbf{r}_1, \mathbf{r}_2) = \sum'_\mu v_\mu^2 \phi_\mu^*(\mathbf{r}_1) \phi_\mu(\mathbf{r}_2), \quad \alpha \equiv p, n. \quad (11)$$

A solid dot indicates a point in r space that is integrated, while the empty dot is the point where the density is calculated.

Due to the orthonormality of the s.p. wave functions, the IPM density matrices satisfy the property

$$\int d^3 r' \rho_\alpha^{\text{IPM}}(\mathbf{r}_1, \mathbf{r}') \rho_\alpha^{\text{IPM}}(\mathbf{r}', \mathbf{r}_2) = \rho_\alpha^{\text{IPM}}(\mathbf{r}_1, \mathbf{r}_2). \quad (12)$$

Because of this, the integration on the open dots in the diagrams of Fig. 1 implies that, in absolute value, the contributions of the diagrams (b) and (d) are equal, as well as those of the diagrams (c) and (e). For this reason, the integral on \mathbf{r} of the correlated terms cancel exactly, and the correlated density

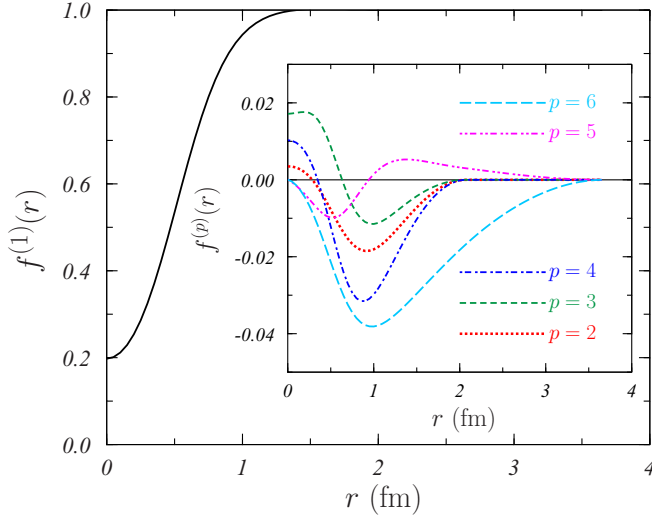


FIG. 2. The SRC functions $f^{(1)}$ and $f^{(p)}$ ($p = 2, \dots, 6$), Eq. (6), for the six operator channels considered in our calculations.

is normalized as the IPM one:

$$\int d^3r \rho_\alpha^{\text{SRC}}(\mathbf{r}) = \int d^3r \rho_\alpha^{\text{IPM}}(\mathbf{r}). \quad (13)$$

These integrals are equal to A , Z , or N depending on the density distribution considered. We indicate with $\rho(\mathbf{r})$ the diagonal part of the one-body density matrix. It is worth remarking on the need to consider all the diagrams of Fig. 1, i.e., those with two and three points, in order to conserve the proper normalization of the correlated density.

Explicit expressions of the contribution of the diagrams in terms of the radial s.p. wave functions are given in Ref. [15]. The only difference in the present calculations is the presence of the v^2 occupation probability multiplying every pair of s.p. wave functions.

The two-body correlation scalar functions are the only physics input which is not consistently derived from the selected effective nucleon-nucleon interaction. We present here the results obtained by using the $f^{(p)}(r_{ij})$ taken from a Fermi hypernetted-chain calculation for the ^{48}Ca nucleus [17], carried out with the microscopic V8' Urbana interaction [16] (see Fig. 2). We have tested the effects of other correlation functions presented in Ref. [17] related to other doubly magic nuclei and to nuclear matter, and we did not find remarkable differences with the results presented below.

C. Long-range correlations

The part of the nuclear Hamiltonian not considered by the IPM, the residual interaction, is the source of the so-called long-range correlations (LRC), which take into account collective phenomena inside the nucleus.

We have described the effects of the LRC on the density distributions by extending the model presented in Refs. [18–20]. We have substituted the random phase approximation Y amplitudes with those obtained with the quasiparticle random phase approximation (QRPA) theory. In

this approach, the density distributions can be written as

$$\rho_\alpha^{\text{LRC}}(r) = \rho_\alpha^{\text{IPM}}(r) - \sum_{J^\Pi} \frac{2J+1}{8\pi} \sum_{E_k} \sum'_{\mu < \nu} |Y_{\mu\nu}^{J^\Pi}(E_k)|^2 \times \{[\mathcal{R}_\mu(r)]^2 - [\mathcal{R}_\nu(r)]^2\}, \quad \alpha \equiv p, n. \quad (14)$$

From the above expression emerges the fact that the relevant ingredient modifying the IPM density is provided by the QRPA Y amplitudes calculated for a specific excited state of energy E_k , angular momentum J , and parity Π . Because of the orthonormalization of the s.p. wave functions, an integration on \mathbf{r} produces equal contributions of the two terms related to the same QRPA Y amplitudes, therefore they cancel each other. Also in this case the normalization of ρ^{LRC} is the same as that of ρ^{IPM} .

Our QRPA calculations, whose technical details can be found in Ref. [21], are based on a discrete set of s.p. wave functions, therefore the energy spectrum we obtain is discrete. On the other hand, the three sums in Eq. (15) have to be truncated. The dimensions of the s.p. configuration space, which limit the sum on the states μ and ν and ensure the stability of the QRPA results, are fixed by using the prescriptions described in Ref. [21].

For a given multipolarity J^Π , we have studied the maximum energy required in the sum on E_k to stabilize the result. Even though every excitation multipole, in each of the nuclei investigated, has its own value for this maximum energy E_{max} , we have found that $E_{\text{max}} = 20$ MeV, for all multiplicities included in Eq. (15), ensures sufficient stability of our results.

Concerning the sum on J^Π , we have considered all the positive and negative multipoles with angular momentum from $J = 1$ to $J = 3$ and also the contribution of $J = 0^+$. As the more relevant contributions come from the low-lying excited states, in the case of the ^{42}Ca , ^{44}Ca , and ^{46}Ca isotopes, we have included also the 4^+ and 6^+ multipoles since, in our calculations, some excited states with these multiplicities appear below 4 MeV.

III. RESULTS

In our study we have considered the even-even Ca isotopes. The parameters of the effective nucleon-nucleon interactions have been chosen to provide a good IPM description of the ground state of a set of nuclei all along the nuclear chart [13,22]. As an example of the performances of these interactions, we compare in Table I the experimental binding energies of the nuclei we have investigated [23] with those obtained with our IPM (HF+BCS) by using the three interactions considered. The good agreement between the empirical values and the results of our calculations is evident, and also expected, since binding energies, among other data, have been used to select the values of the force parameters [22].

Since our IPM is built to reproduce some experimental nuclear quantities, the appearance of phenomena beyond IPM can be identified by doing a relative comparison between the theoretical results. On the other hand, the quantity experimentally measured, the isotope shift, is defined in a relative manner as the difference between the square of the charge

TABLE I. Binding energies per nucleon, in MeV, for the Ca isotopes under investigation, obtained with our HF+BCS IPM by using the D1S, D1ST2a, and D1M interactions, compared to the experimental values taken from the compilation by Brookhaven National Laboratory [23]. The largest experimental uncertainty is 0.012 MeV in ^{60}Ca .

A	D1S	D1ST2a	D1M	Expt.
34	7.254	7.255	7.148	7.173
36	7.867	7.871	7.754	7.816
38	8.296	8.296	8.180	8.240
40	8.626	8.624	8.513	8.551
42	8.668	8.669	8.556	8.617
44	8.711	8.718	8.602	8.658
46	8.719	8.732	8.614	8.669
48	8.694	8.714	8.593	8.667
50	8.551	8.572	8.458	8.550
52	8.404	8.427	8.320	8.429
54	8.211	8.230	8.140	8.248
56	8.028	8.033	7.956	8.033
58	7.832	7.834	7.768	7.828
60	7.614	7.620	7.577	7.627

radii of the each Ca isotope and that of ^{40}Ca ,

$$\delta R_{\text{ch}}^2(A) = [R_{\text{ch}}(A)]^2 - [R_{\text{ch}}(A = 40)]^2. \quad (15)$$

These are the two reasons that have induced us to concentrate our study on the isotope shifts rather than on the charge radii.

In Fig. 3(a), we compare the values of the isotope shifts obtained in our IPM calculations, carried out with the three different parametrizations of the Gogny interaction, D1S (red open dots), D1M (blue open squares), and D1ST2a (green solid dots), with the available experimental data of Refs. [1,2,24–26] (black triangles).

The first remark is that the behaviors of our IPM results are very similar, independently of the interaction used. A quantitative indicator of this similarity is the average of the absolute differences between these curves, which is smaller than 0.07 fm^2 , with a maximum value of 0.2 fm^2 (in the case of ^{54}Ca). It is also worth noting that the tensor terms of the force do not play any relevant role: the results obtained with D1ST2a and D1S almost overlap.

The comparison with the experimental data is not straightforward. We observe good agreement with the isotope shifts of the nuclei lighter than ^{40}Ca and heavier than ^{48}Ca , while in the cases of ^{42}Ca , ^{44}Ca , and ^{48}Ca the IPM fails to describe the data. The IPM isotope shifts increase smoothly with increasing neutron number. In contrast, the experimental data show a steeper increase from ^{40}Ca up to the value of ^{44}Ca and a decreasing behavior for ^{46}Ca and ^{48}Ca , whose isotope shift is almost zero.

A direct comparison between the r.m.s. radii obtained by using our IPM densities, as indicated by Eq. (1), and the empirical ones is shown in Fig. 3(b). The latter values have been obtained from Eq. (15) by considering the experimental isotope shifts and the reference value $R_{\text{ch}}(A = 40) = 3.4776(19) \text{ fm}$ [27].

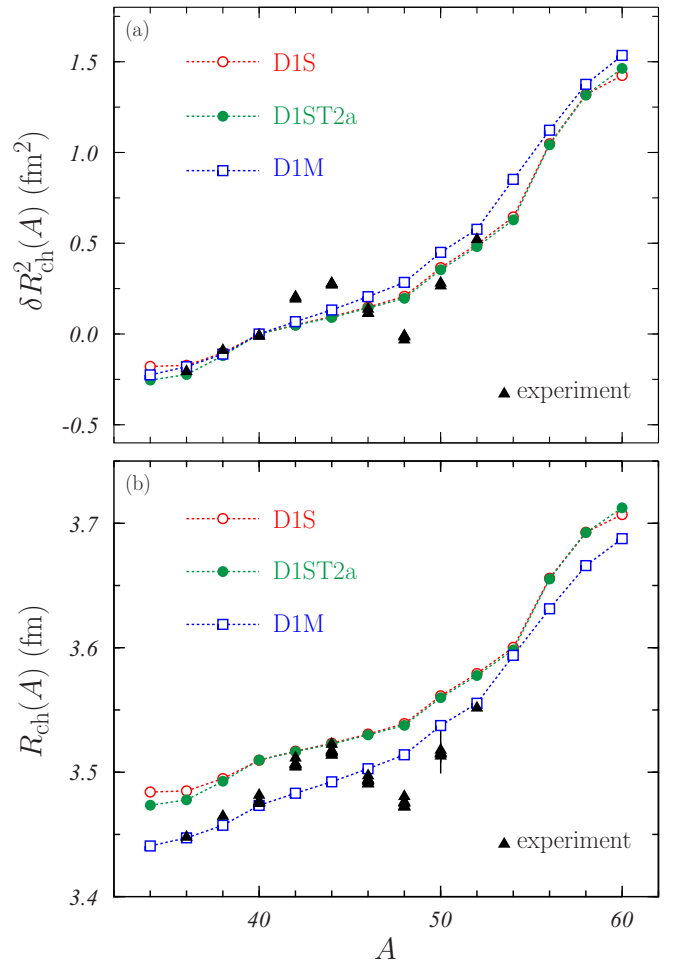


FIG. 3. IPM results obtained with the D1S (open red dots), D1ST2a (solid green dots), and D1M (open blue squares) Gogny interactions for the Ca isotopes considered in our work, with the experimental data (black triangles). (a) Isotope shifts of the squared r.m.s. charge radii evaluated with respect to the ^{40}Ca r.m.s. radius, Eq. (15); the experimental data were obtained from Refs. [1,2,24–26]. (b) r.m.s. charge radii of the Ca isotopes; the experimental values were calculated by considering the experimental isotope shifts shown in panel (a) and the reference r.m.s. charge radius $R_{\text{ch}}(A = 40) = 3.4776(19) \text{ fm}$ [27].

The D1S and D1ST2a results are almost overlapping, with differences smaller than 0.5%, and this indicates again that the tensor terms in the interaction do not produce noticeable effects on the charge radii.

We observe a systematic difference, of about 1%, between the results obtained with the D1S and the D1M interactions, the latter one producing smaller values. This difference improves the description of the data obtained with the D1M force with respect to the D1S and D1ST2a interactions. We remark that in the set of empirical information used to select the parameters of the D1M force, the charge radii values of 707 nuclei were considered [13]. This is probably the reason for the better agreement with the experiment obtained with the D1M interaction.

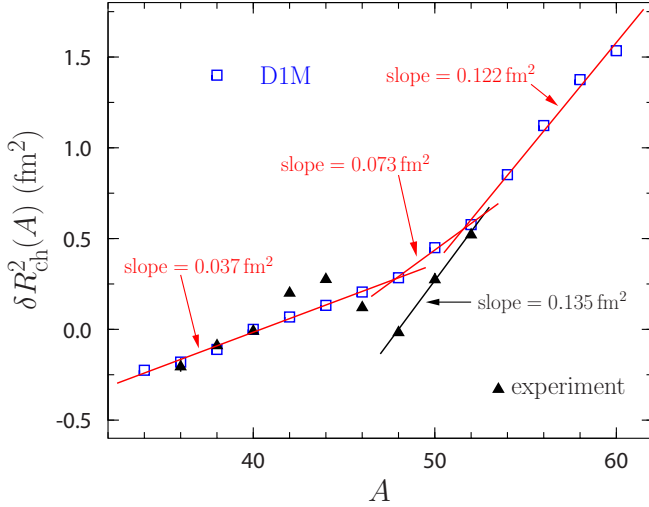


FIG. 4. Isotope shifts, Eq. (15), obtained in the IPM calculations with the DIM interaction (open blue squares) and experimental results of Refs. [1,2,24–26] (solid black dots). The linear fits to the three sections of the IPM results and to the experimental values for the heavier Ca isotopes are indicated by the straight lines. The angular coefficients, i.e., slopes, of these lines are also given.

In any case, it is very striking that all the IPM calculations fail to describe the charge radius of ^{48}Ca , a doubly magic nucleus, and, in general, the charge radii of the nuclei between ^{40}Ca and ^{48}Ca . This is a well known problem since 1968 [28], and it has been shown to be present in different kinds of IPMs (see for example the results of Refs. [29–31]).

The behavior of the isotopes shifts that we have obtained with our IPM can be separated into three regions. As example of this analysis, we show again in Fig. 4 the comparison between the isotope shifts obtained with the DIM interaction (blue open squares) and the experimental values (black solid triangles). These latter values are the average of those quoted by different experiments [1,2,24–26]. The red lines of the figure are the results of linear fits of the DIM data for three regions: nuclei lighter than ^{48}Ca , from ^{48}Ca to ^{52}Ca , and nuclei heavier than ^{52}Ca . The values of the angular coefficients, i.e., the slopes, of these lines are also indicated in the figure. Similar results are obtained for the other two forces considered.

We identify three regions also in the case of the experimental data, but, in this case, the trend is remarkably different from that found for the IPM. The behavior of the data for the isotopes lighter than ^{40}Ca and heavier than ^{48}Ca is linear. The value of the slope of the line fitting this latter set of data is very similar to that of the IPM results for nuclei heavier than ^{54}Ca . The real problem is related to the experimental data of the Ca isotopes from ^{40}Ca to ^{48}Ca . Contrary to the IPM results, these data present a maximum for the ^{44}Ca nucleus, and a minimum for the ^{48}Ca that, as we have already pointed out, shows a null isotope shift, indicating that its charge r.m.s. radius is essentially the same as that of ^{40}Ca .

The inclusion of the correlations modifies the IPM charge distributions and, consequently, the values of the charge r.m.s. radii. The effects of the SRC are mainly concentrated in

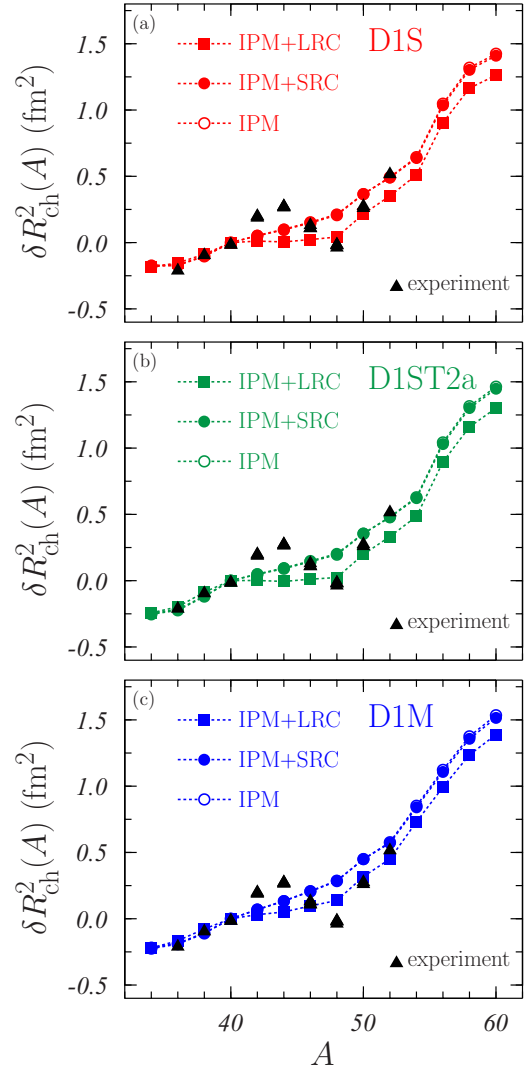


FIG. 5. Effect of the short- and long-range correlations on the isotope shifts, defined in Eq. (15). The IPM results (open circles) are compared to those found after adding SRC (solid circles) and LRC (solid squares). Results for the D1S (a), D1ST2a (b), and D1M (c) interactions are shown. Experimental data of Refs. [1,2,24–26] are indicated by solid black triangles.

the nuclear interior, therefore the IPM radii are only slightly modified. Equation (1) clearly indicates that the values of the r.m.s. radii are obtained by integrating the densities weighted by a factor r^4 , against a factor r^2 related to the normalization. For this reason, the radii are more sensitive to the changes of the nuclear surface than those of the interior. The LRC, which consider the coupling of the IPM ground state with low-lying surface collective excitations, enlarge the charge distributions and increase the values of the r.m.s radii by about 15%.

The effects of the correlations on the isotope shifts defined in Eq. (15) are shown in Fig. 5. The three panels present, separately, the results obtained for the three interactions considered. In each panel the open circles indicate the IPM results, the solid circles those obtained by considering the SRC, and the solid squares those including the LRC.

The effects of the SRC are extremely small, and the results obtained by taking them into account almost overlap with those of the IPM. In contrast, the LRC produce a significant modification of the overall trend.

In the isotopes lighter than ^{40}Ca , the LRC effects are negligible. However, already the IPM values describe well the corresponding experimental data.

The largest effects of the LRC are seen in the nuclei between ^{40}Ca and ^{48}Ca . The inclusion of the LRC generates a set of almost constant values for the D1S and D1ST2a interactions, while for the DIM interaction we found a moderate growth, though much smaller than that shown by the IPM results. The important point is that by including LRC a good description of the ^{48}Ca isotope shift for the D1S and D1ST2a interactions is obtained. The value found for the DIM interaction is not as good, but certainly much better than that of the IPM.

Above ^{48}Ca , the trend of the isotope shift is roughly the same as in the IPM calculations, showing an enhancement with two well defined slopes for $A < 52$ and $A > 52$, respectively. For the nuclei heavier than this isotope, the growth rate of the isotope shifts is similar to the experimental one, as determined from the values of ^{48}Ca , ^{50}Ca , and ^{52}Ca .

IV. DISCUSSION AND CONCLUSIONS

In this work, we have presented the results of our study of the isotope shifts of even-even Ca isotopes. We first carried out IPM calculations, based on a HF+BCS approach, by using three finite-range effective interactions. The HF and BCS steps of our calculations were executed by consistently using the same interaction. The results obtained do not show any particular sensitivity to the interaction used, especially to the presence of tensor terms. These IPM results agree with the experimental values for the lighter Ca isotopes (with $A \leq 40$) and describe the growth rate of the heavier ones (with $A \geq 50$). The problem is the failure in describing the behavior of the experimental data of the nuclei from ^{40}Ca to ^{48}Ca , in particular the fact that these two doubly magic nuclei, which in principle should be well described by the IPM, have the same charge radius. We did not find remarkable effects generated by the pairing, contrary to what has been claimed in Ref. [32].

We have extended our calculations by including short- and long-range correlations. The effects of the SRC, treated by using the model of Ref. [15], are irrelevant. This result disagrees with the findings of Ref. [33]. However, we found it difficult to make a direct comparison between our and their definition

of SRC and, therefore, to compare the specific contributions taken into account in both calculations. We remark that the fully microscopic calculation of Ref. [34] gives the correct proton radius of ^{48}Ca .

More significant are the effects of the LRC which we have described by extending the model of Ref. [20] in order to consider QRPA backward amplitudes. The LRC do not affect the behavior of the IPM in the region of the light and heavy Ca isotopes where the IPM provides already a good description of the data. The results of the intermediate region between ^{40}Ca and ^{48}Ca are strongly modified. The first, important point is that with the inclusion of LRC we obtain the same radii for the two doubly magic nuclei. The results are better for the D1S and D1ST2a forces than for the DIM, but also in this latter case the improvement with respect to the IPM is evident.

The second point is that, for this set of isotopes, the LRC calculations generate almost constant values of the isotope shifts, contrary to the IPM results which show a continuous increase. Despite of a clear improvement, the trend of the experimental data, showing a maximum for ^{44}Ca , is not yet well described.

In Ref. [35] the authors pointed out the need to include terms related to proton and neutron magnetic moments and spin-orbit in order to obtain a precise description of isotope shifts. These effects are very small, and, furthermore, they show a linear trend in the region between ^{40}Ca and ^{48}Ca , therefore they are unable to explain the behavior of the experimental results.

A good description of the data in the region of interest is provided by the shell model calculation of Ref. [36]. By using our language, we may say that in this approach the LRC have been taken into account in a wider manner by including effects beyond the single-quasiparticle excitations, which are the only ones considered in our QRPA calculations.

In conclusion, there is no problem in describing the new isotope shift data measured for neutron rich Ca isotopes, and the data in the region between the two doubly magic isotopes ^{40}Ca and ^{48}Ca indicate the relevance of the LRC.

ACKNOWLEDGMENTS

This work has been partially supported by the Junta de Andalucía (FQM387), the Spanish Ministerio de Economía y Competitividad (PID2019-104888GB-I00) and the European Regional Development Fund (ERDF). One of us (G.C.) thanks Sonia Bacca for useful discussions.

[1] R. F. Garcia Ruiz *et al.*, *Nat. Phys.* **12**, 594 (2016).
 [2] A. J. Miller *et al.*, *Nat. Phys.* **15**, 432 (2019).
 [3] M. Tanaka *et al.*, *Phys. Rev. Lett.* **124**, 102501 (2020).
 [4] S. A. Fayans, S. V. Tolokonnikov, E. L. Trykov, and D. Zawischa, *Nucl. Phys. A* **676**, 49 (2000).
 [5] P. Klüpfel, P.-G. Reinhard, T. J. Bürvenich, and J. A. Maruhn, *Phys. Rev. C* **79**, 034310 (2009).

[6] P.-G. Reinhard and W. Nazarewicz, *Phys. Rev. C* **95**, 064328 (2017).
 [7] B. Povh, K. Rith, C. Scholz, and F. Zetche, *Teilchen und Kerne: Eine Einführung in die Physicalischen Konzepte* (Springer, Berlin, 1993).
 [8] M. Anguiano, A. M. Lallena, G. Co', and V. De Donno, *J. Phys. G* **41**, 025102 (2014).

- [9] M. Anguiano, A. M. Lallena, G. Co', and V. De Donno, *J. Phys. G* **42**, 079501 (2015).
- [10] A. R. Edmonds, *Angular Momentum in Quantum Mechanics* (Princeton University Press, Princeton, 1957).
- [11] J. Dechargé and D. Gogny, *Phys. Rev. C* **21**, 1568 (1980).
- [12] J. F. Berger, M. Girod, and D. Gogny, *Comput. Phys. Commun.* **63**, 365 (1991).
- [13] S. Goriely, S. Hilaire, M. Girod, and S. Péru, *Phys. Rev. Lett.* **102**, 242501 (2009).
- [14] M. Anguiano, M. Grasso, G. Co', V. De Donno, and A. M. Lallena, *Phys. Rev. C* **86**, 054302 (2012).
- [15] G. Co', *Nuovo Cimento A* **108**, 623 (1995).
- [16] R. B. Wiringa, V. G. J. Stoks, and R. Schiavilla, *Phys. Rev. C* **51**, 38 (1995).
- [17] F. Arias de Saavedra, C. Bisconti, G. Co', and A. Fabrocini, *Phys. Rep.* **450**, 1 (2007).
- [18] D. J. Rowe, *Nuclear Collective Motion* (Methuen, London, 1970).
- [19] H. Lenske and J. Wambach, *Phys. Lett. B* **249**, 377 (1990).
- [20] M. Anguiano and G. Co', *J. Phys. G* **27**, 2109 (2001).
- [21] V. De Donno, G. Co', M. Anguiano, and A. M. Lallena, *Phys. Rev. C* **95**, 054329 (2017).
- [22] F. Chappert, Nouvelles paramétrisation de l'interaction nucléaire effective de Gogny, Ph.D. thesis, Université de Paris-Sud XI (France), 2007 (unpublished), <http://tel.archives-ouvertes.fr/tel-001777379/en/>
- [23] Brookhaven National Laboratory, National Nuclear Data Center, <http://www.nndc.bnl.gov/>
- [24] H. D. Wohlfahrt, E. B. Shera, M. V. Hoehn, Y. Yamazaki, and R. M. Steffen, *Phys. Rev. C* **23**, 533 (1981).
- [25] C. W. P. Palmer *et al.*, *J. Phys. B* **17**, 2197 (1984).
- [26] L. Vermeeren, R. E. Silverans, P. Lievens, A. Klein, R. Neugart, Ch. Schulz, and F. Buchinger, *Phys. Rev. Lett.* **68**, 1679 (1992).
- [27] I. Angeli and K. P. Marinova, *At. Data Nucl. Data Tables* **99**, 69 (2013).
- [28] R. F. Frosch *et al.*, *Phys. Rev.* **174**, 1380 (1968).
- [29] Y. Aboussir, J. M. Pearson, A. Dutta, and F. Tondeur, *Nucl. Phys. A* **549**, 155 (1992).
- [30] T. R. Werner *et al.*, *Nucl. Phys. A* **597**, 327 (1996).
- [31] H. Nakada, *Phys. Rev. C* **100**, 044310 (2019).
- [32] R. An, L.-S. Geng, and S.-S. Zhang, *Phys. Rev. C* **102**, 024307 (2020).
- [33] G. A. Miller *et al.*, *Phys. Lett. B* **793**, 360 (2019).
- [34] G. Hagen *et al.*, *Nat. Phys.* **12**, 186 (2016).
- [35] P.-G. Reinhard and W. Nazarewicz, *Phys. Rev. C* **103**, 054310 (2021).
- [36] E. Caurier *et al.*, *Phys. Lett. B* **522**, 240 (2001).